POLITECNICO DI TORINO
Repository ISTITUZIONALE

Automatic dynamic range estimation for ultrasound image visualization and processing

Original
Automatic dynamic range estimation for ultrasound image visualization and processing / Meiburger, K.M., Seoni, S., Matrone, G.. - 2020-:(2020), pp. 1-4. (2020 IEEE International Ultrasonics Symposium, IUS 2020 Virtual September 6-11 2020) [10.1109/IUS46767.2020.9251470].

Availability:
This version is available at: 11583/2860150 since: 2021-01-09T16:42:39Z

Publisher:
IEEE Computer Society

Published
DOI:10.1109/IUS46767.2020.9251470

Terms of use:

This article is made available under terms and conditions as specified in the corresponding bibliographic description in the repository

Publisher copyright
IEEE postprint/Author's Accepted Manuscript

©2020 IEEE. Personal use of this material is permitted. Permission from IEEE must be obtained for all other uses, in any current or future media, including reprinting/republishing this material for advertising or promotional purposes, creating new collecting works, for resale or lists, or reuse of any copyrighted component of this work in other works.

(Article begins on next page)

11 September 2026

Automatic Dynamic Range Estimation for Ultrasound Image Visualization and Processing

Kristen M. Meiburger
Polito[BIO]Med Lab, Biolab, Dept. of Electronics and Telecommunications
Politecnico di Torino
Torino, Italy
kristen.meiburger@polito.it

Silvia Seoni
Polito[BIO]Med Lab, Biolab, Dept. of Electronics and Telecommunications
Politecnico di Torino
Torino, Italy
silvia.seoni@polito.it

Giulia Matrone
Bioengineering Lab., Dept. of Electrical, Computer and Biomedical Engineering
University of Pavia
Pavia, Italy
giulia.matrone@unipv.it

***Abstract*—Numerous beamforming methods exist for ultrasound B-mode imaging, but it is known that adaptive/non-linear beamformers may alter the image dynamic range. To obtain an 8-bit image for further processing, it is necessary to determine a specific dynamic range, which may vary between beamforming methods in order to obtain a visually similar image. The aim here is to present an automated method to estimate the optimal dynamic range. We tested two phantom images and one *in vivo* image using six different beamforming techniques. The cumulative sums of the image histograms are compared with a standard dynamic range (i.e., 60 dB) and the contrast ratio and contrast-to-noise ratio are computed. We show that the automatically determined dynamic range is able to standardize the image among various beamforming techniques, which is essential when further image processing methods are employed.**

Keywords—ultrasound beamforming, dynamic range, image processing, automatic

I. Introduction

Over the last couple decades, numerous beamforming methods for ultrasound B-mode imaging have been presented and studied [1]–[3], showing a higher contrast and better resolution when compared to the conventional delay-and-sum (DAS) beamforming technique [3], [4]. Recently, it has been shown that adaptive and non-linear beamformers may alter the image dynamic range [5], [6]. This dynamic range alteration typically also reports an improvement of the contrast measurements, which could however be due simply to the stretching of the dynamic range for some beamformers [5].

Many semi-automatic or completely automatic segmentation algorithms exist in literature for B-mode ultrasound images [7], and another common application in ultrasound imaging is texture analysis, which takes into consideration pixel intensity values and their spatial relationship [8], [9]. These methods are in the vast majority done on 8-bit ultrasound images [10]–[12]. In order to obtain an 8-bit image for subsequent image processing, a dynamic range must be determined for image display and the image values outside of the determined range must then be cut. The remaining values are then rescaled to values between 0 and 255. Therefore, in order to obtain images from different beamforming techniques that visually appear similar, it is necessary to match histograms, which is typically done manually. This is due to the fact that using the same standard dynamic range for different beamforming methods produces images that are visually quite different (Fig. 1). Here, we present an automated method to estimate the optimal dynamic range that matches the histograms of images obtained with various beamforming methods.

II. Background

In this section we describe the 6 beamforming techniques examined here. More detailed descriptions of the beamforming methods and parameters used can be found in [1], [4].

A. Conventional Delay-and-Sum Beamforming

To reconstruct an ultrasound image, the raw radiofrequency (RF) signals $\hat{s}_i(t)$, with i=1…N, received by the N elements in the active aperture, must first be properly focused by applying a set of focusing delays (τ_i) and then summed. This procedure is called Delay and Sum (DAS) beamforming, written as:

$$y_{DAS}(t) = \sum_{i=1}^{N} \hat{s}_i(t-\tau_i) = \sum_{i=1}^{N} s_i \tag{1}$$

where y_{DAS} is the DAS-beamformed output signal.

B. Coherence-Based Beamformers

In this work, 5 different beamformers, all based on the concept of spatial coherence of backscattered echoes, were also implemented. The first is the Filtered Delay Multiply and Sum (FDMAS) algorithm proposed in [1], which computes the beamformed signal y_{FDMAS} as:

$$y_{FDMAS}(t) = BPfilter\left\{\sum_{i=1}^{N-1}\sum_{j=i+1}^{N} sign(s_i(t)s_j(t))\cdot\sqrt{|s_i(t)s_j(t)|}\right\} \tag{2}$$

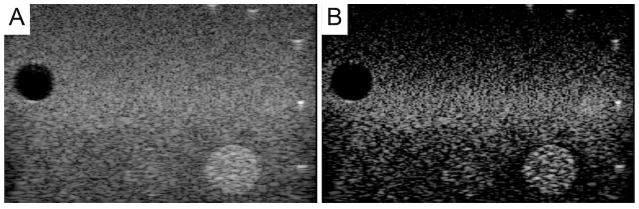

Fig. 1. Example image obtained using the same standard 60 dB dynamic range for (A) DAS and (B) CF beamformers.

where *BPfilter* denotes a band-pass filter at twice the transmit frequency.

The other implemented algorithms were the coherence factor (CF) [13], generalized CF (GCF) [2], phase and sign CF (PCF and SCF) [14]. Differently from FDMAS, all these techniques compute a weighting matrix which is then applied to the DAS beamformed image as follows:

$$y_{CF}(t) = y_{DAS}(t) \cdot CF(t) = y_{DAS}(t) \cdot \frac{\left|\sum_{i=1}^{N} s_i(t)\right|^2}{N\sum_{i=1}^{N}|s_i(t)|^2}, \quad (3)$$

$$y_{GCF}(t) = y_{DAS}(t) \cdot GCF(t) = y_{DAS}(t) \cdot \frac{\sum_{k=0}^{M_0}|S(k,t)|^2}{\sum_{k=0}^{N-1}|S(k,t)|^2}, \quad (4)$$

$$y_{PCF}(t) = y_{DAS}(t) \cdot PCF(t) = y_{DAS}(t) \cdot \max\{0,\ 1 - \frac{\gamma}{\pi/\sqrt{3}}\sigma(\varphi_i(t))\}, \quad (5)$$

$$y_{SCF}(t) = y_{DAS}(t) \cdot SCF(t) = y_{DAS}(t) \cdot |1 - \sigma(b_i(t))|^p, \quad (6)$$

where k represents the spatial frequency index, $S(k)$ is the spectrum of $s_i(t)$, M_0 is a spatial frequency threshold, γ and p are two user-defined parameters which tune the sensitivity of PCF and SCF, respectively, $\sigma(\varphi_i(t))$ is the standard deviation of the signal instantaneous phases $\varphi_i(t)$, and $b_i(t) = \text{sign}(s_i(t))$.

In all the presented cases, the final image in dB scale is obtained after enveloped-detection, normalization and log-compression of the beamformed signals.

III. Materials and Methods

To evaluate the effectiveness of the automatic dynamic range estimation, tests were done both on phantom ultrasound images and one *in vivo* ultrasound image. In particular, two phantom (model 040GSE, CIRS Inc, USA) images were acquired using a linear array probe (model LA533, Esaote s.p.a., Florence, Italy) working at 5 MHz and a phased array probe (model PA230, Esaote) at 2 MHz. Furthermore, one *in vivo* image of the carotid artery was acquired using again the LA533 linear array probe, this time working at 7 MHz. The probes were connected to the 64-channel ULA-OP system [15]. A 64-element aperture was used in transmission and reception (in the phased-array case, only its odd elements were employed). The transmitted signal was a 2-cycle, Hanning-tapered sinusoid at the central frequencies mentioned above for the three considered tests. During phantom/carotid acquisitions with the linear probe, the transmit focal depth was set to 20 mm and 25 mm, respectively, while for phased array scans the focus was set at 70 mm. In reception, dynamic focusing was always applied, and 192 scan lines were acquired.

Once the raw RF signals were acquired and sampled at 50 MHz, the six different beamforming techniques described in the Background section were used to reconstruct the image in Matlab (The MathWorks, Natick, MA, USA), setting γ=p=0.8 and M_0=2. In order to automatically determine the dynamic range with which to both visualize and generate the 8-bit image, the probability density function of the log-compressed values of the beamformed signals is computed over 256 bins. Subsequently, the weighted mean of the histogram is found (pdf_{wm}). The final optimal dynamic range (DR) is then computed according to the following formula:

$$\text{DR} = \text{pdf}_{\text{wm}} + \alpha * \text{pdf}_{\text{wm}} \quad (7)$$

where $\alpha = 0.2$ in the case of the *in vivo* carotid artery image, and $\alpha = 0.5$ for the phantom images. The DR is then rounded to the nearest five to obtain the final dynamic range. The upper limit of the image dB scale is always equal to 0 dB, so the lower limit is therefore equal to -DR. The [-DR 0] dB scale is then converted to an 8-bit scale [0 255].

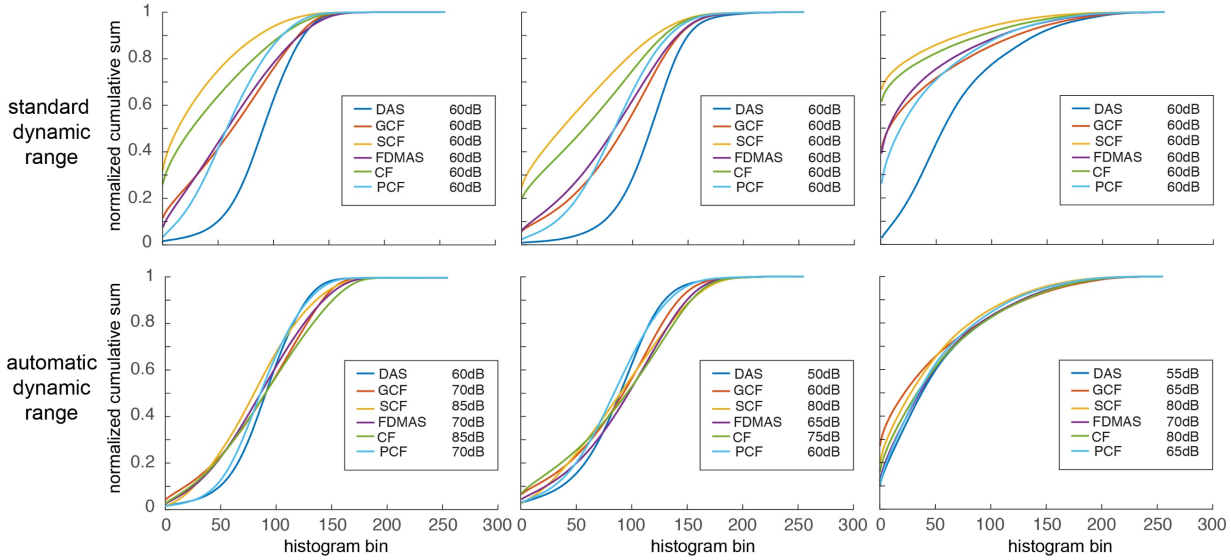

Fig. 2. Image histogram cumulative sum results. Top row: cumulative sum of image histograms obtained using standard 60 dB dynamic range. Bottom row: cumulative sum of image histograms obtained using automatically determined dynamic range.

TABLE I. AUTOMATICALLY DETERMINED DYNAMIC RANGE VALUES

	DAS [dB]	FDMAS [dB]	CF [dB]	GCF [dB]	SCF [dB]	PCF [dB]
Phantom (linear array)	60	70	85	70	85	70
Phantom (phased-array)	50	65	75	60	80	60
In-vivo carotid (linear array)	55	70	80	65	80	65

Qualitatively, the 8-bit images obtained with the automatic dynamic range were visually evaluated to determine if the images resembled each other in terms of average gray level and were compared with those obtained using a standard 60 dB dynamic range.

For a quantitative evaluation, two methods were used. First, the cumulative sum of the obtained 8-bit image histograms was computed using both the automatically determined dynamic range and the standard 60 dB dynamic range. The cumulative sums are plotted and the trend between beamforming techniques is evaluated. Secondly, the contrast ratio (CR) and contrast-to-noise ratio (CNR) were computed on manually placed Regions-Of-Interest (ROIs) on the grayscale images (0-255) obtained using the automatic and standard dynamic range. The definitions used of CR and CNR are as follows:

$$CR_{gray} = \left|\bar{\mu}_{ROI} - \bar{\mu}_{B}\right| \tag{8}$$

$$CNR_{gray} = \frac{\left|\bar{\mu}_{ROI} - \bar{\mu}_{B}\right|}{\sqrt{\bar{\sigma}^2_{ROI} + \bar{\sigma}^2_{B}}} \tag{9}$$

where $\bar{\mu}$ is the mean of the re-scaled log-compressed grayscale values within the ROI and background (B) regions, and $\bar{\sigma}^2$ is the variance of the grayscale values again within the ROI and B regions. The subscript *gray* denotes that the metrics are computed on the re-scaled grayscale (0-255) image values.

IV. RESULTS

Table 1 shows the automatically computed dynamic ranges for each image and beamforming method. The cumulative sums of the image histograms are portrayed in Fig. 2, where the second and third row portray the cumulative sum of the image histograms using the standard and automatic dynamic range, respectively. Fig. 3 shows the image of the phantom acquired with the linear array beamformed using the CF (top row) and GCF (bottom row) techniques, where the left and right columns show the images visualized with a standard dynamic range and the automatic dynamic range, respectively. Similarly, Fig. 4 displays the phantom image acquired with the phased array probe and beamformed with DAS (top row) and SCF (bottom row) methods, and Fig. 5 portrays in the top and bottom rows the *in vivo* carotid artery image beamformed with the FDMAS and PCF techniques, respectively.

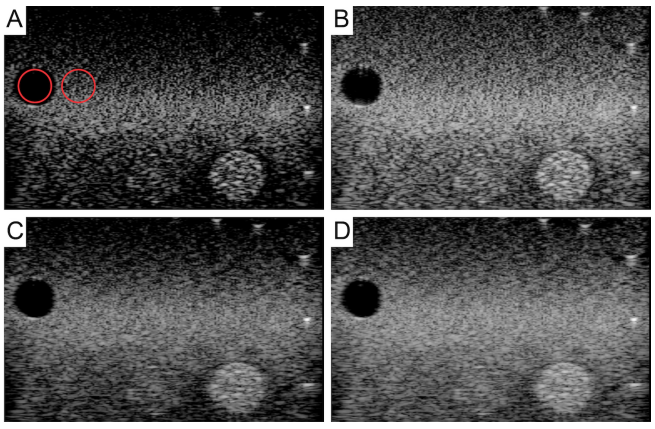

Fig. 3. Phantom image (linear array) beamformed using CF (A, B) and GCF (C, D) with standard (A, C) and automatic dynamic range (B, D). The ROIs used for CR and CNR calculations are in red.

TABLE II. CONTRAST RATIO (CR) AND CONTRAST-TO-NOISE RATIO (CNR) FOR ROIS DEPICTED IN FIG. 3, 4, 5.

		DAS	FDMAS	CF	GCF	SCF	PCF
Phantom (linear array)	CR_{auto}	26.10	31.31	38.76	33.25	32.36	28.71
	CR_{60}	26.10	21.69	15.66	23.33	10.95	19.30
	CNR_{auto}	4.65	3.11	2.99	4.97	2.44	3.72
	CNR_{60}	4.65	2.27	1.47	3.56	1.11	2.64
Phantom (phased-array)	CR_{auto}	17.62	29.17	36.77	25.39	39.13	24.12
	CR_{60}	19.75	26.30	24.34	25.39	22.19	24.12
	CNR_{auto}	3.32	3.40	3.72	3.66	3.41	3.25
	CNR_{60}	2.91	3.35	2.86	3.66	2.35	3.25
In vivo carotid (linear array)	CR_{auto}	20.40	26.31	29.27	26.62	27.67	23.43
	CR_{60}	21.21	22.55	19.86	23.67	15.61	21.30
	CNR_{auto}	2.99	2.59	2.56	2.91	2.50	2.87
	CNR_{60}	2.83	2.66	2.29	2.83	1.97	2.92

The CR and CNR values obtained using the ROIs in red shown in Figs. 3, 4, and 5 are reported in Table 2.

V. DISCUSSION

As can be seen in the middle row of Fig. 2, the image histogram cumulative sum follows different trends when a standard dynamic range is used, but it follows similar trends when the automatically determined dynamic range is employed. This shows how the proposed method is able to match histograms between beamforming techniques in an efficient and effective way.

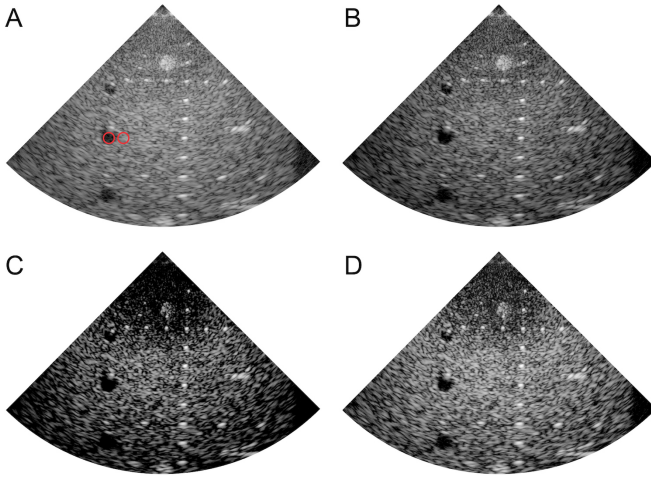

Fig. 4. Phantom image (phased array) beamformed using DAS (A, B) and SCF (C, D) with standard (A, C) and automatic dynamic range (B, D). The ROIs used for CR and CNR calculations are in red.

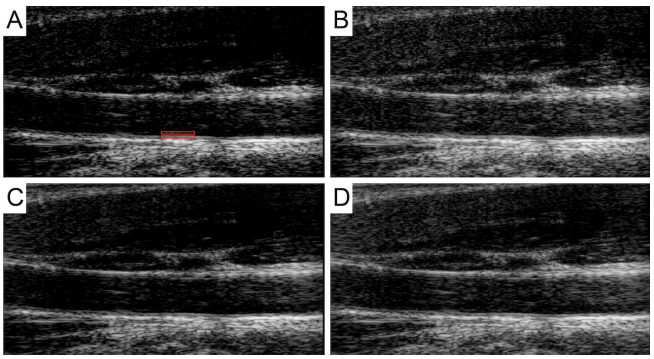

Fig. 5. *In vivo* carotid image beamformed using FDMAS (A, B) and PCF (C, D) with standard (A, C) and automatic dynamic range (B, D). The ROIs used for CR and CNR calculations are in red.

Overall, our results show that, even after matching the histograms, the images obtained with coherence-based beamformers preserve their higher quality with respect to DAS beamforming. This demonstrates that the coherence-based beamformers do in fact provide an improvement compared to DAS that is not simply due to dynamic range rescaling. Indeed, the CR values obtained using the coherence-based beamformers are always higher than those obtained with DAS when considering the automatically determined dynamic range. On the other hand, the same cannot be said for the CNR, which can be attributed to the fact that different beamformers alter speckle statistics [16]. In particular, it can be appreciated how in many of the coherence-based beamformed images, there is a higher variance within the ROIs when compared to DAS, therefore increasing the CNR denominator and lowering the final obtained value. Moreover, both the CR and CNR values increase when using the automatic DR compared to the standard DR (Tab. 2). In a couple of cases, the CR values decrease while the CNR values increase, but this is only observed using the DAS beamforming method. Similarly, the CNR values show slightly lower values (< 0.1 difference) while the CR values are higher in two cases (FDMAS and PCF), which is observed only in the *in vivo* carotid artery image. This minimal difference can be explained by the fact that, when considering a smaller dynamic range, the overall image takes on lower values (i.e., the image is darker), since more log-compressed values are cut and rescaled to 0. For the *in vivo* carotid artery image, a smaller dynamic range decreases signals within the artery lumen (Fig. 5), which causes the variance within the background ROI to decrease.

Two further considerations need to be done regarding the present study. First of all, the automatic method determines the dynamic range taking for granted the fact that an upper limit equal to 0 dB is suitable. An upper limit of 0 dB may not be ideal for all images, and further studies need to be done to take this aspect into consideration and to determine how the upper limit may also be automatically determined, if necessary. Secondly, the automatically determined dynamic range is based on the weighted mean, which once calculated must then be added to the weighted mean multiplied by a scale factor (i.e., α), as shown in (7). In this study, it was found that α may vary between different images and was determined empirically by testing various values for each image. Importantly, however, the value of α is the same for every beamforming technique. Hence, to use the method in future studies with different images, it may be necessary to tune α. However, once it is determined for one beamforming method (e.g., the standard DAS), it can be effectively employed for all other beamforming techniques.

VI. Conclusion

We have presented here a simple yet effective method for automatically determining the dynamic range of ultrasound images obtained using different beamforming algorithms. We showed how the automatic method standardizes the 8-bit image among the six analyzed beamformers, which is essential when further image processing methods, such as segmentation and texture features, are employed.

References

[1] G. Matrone, A. S. Savoia, G. Caliano, and G. Magenes, "The Delay Multiply and Sum Beamforming Algorithm in Ultrasound B-Mode Medical Imaging," *IEEE Trans. Med. Imaging*, vol. 34, no. 4, pp. 940–949, Apr. 2015.

[2] P. C. Li and M. L. Li, "Adaptive imaging using the generalized coherence factor," *IEEE Trans. Ultrason. Ferroelectr. Freq. Control*, vol. 50, no. 2, pp. 128–141, Feb. 2003.

[3] J. F. Synnevåg, A. Austeng, and S. Holm, "Adaptive beamforming applied to medical ultrasound imaging," *IEEE Trans. Ultrason. Ferroelectr. Freq. Control*, vol. 54, no. 8, pp. 1606–1613, 2007.

[4] G. Matrone, A. Ramalli, J. D'Hooge, P. Tortoli, and G. Magenes, "A Comparison of Coherence-Based Beamforming Techniques in High-Frame-Rate Ultrasound Imaging with Multi-Line Transmission," *IEEE Trans. Ultrason. Ferroelectr. Freq. Control*, vol. 67, no. 2, pp. 329–340, 2020.

[5] O. M. H. Rindal, A. Austeng, A. Fatemi, and A. Rodriguez-Molares, "The Effect of Dynamic Range Alterations in the Estimation of Contrast," *IEEE Trans. Ultrason. Ferroelectr. Freq. Control*, vol. 66, no. 7, pp. 1198–1208, 2019.

[6] A. Rodriguez-Molares *et al.*, "The Generalized Contrast-to-Noise Ratio: A Formal Definition for Lesion Detectability," *IEEE Trans. Ultrason. Ferroelectr. Freq. Control*, vol. 67, no. 4, pp. 745–759, 2020.

[7] K. M. Meiburger, U. R. Acharya, and F. Molinari, "Automated localization and segmentation techniques for B-mode ultrasound images: A review," *Comput. Biol. Med.*, vol. 92, pp. 210–235, Jan. 2018.

[8] M. Galloway, "Texture analysis using grey level run lengths," *Comp Graph. Image Process*, vol. 4, pp. 172–179, 1975.

[9] R. M. Haralick, K. Shanmugam, and I. Dinstein, "Textural Features for Image Classification," *IEEE Trans. Syst. Man. Cybern.*, vol. SMC-3, no. 6, pp. 610–621, Nov. 1973.

[10] K. M. Meiburger *et al.*, "Quantitative analysis of patellar tendon abnormality in asymptomatic professional 'Pallapugno' players: A texture-based ultrasound approach," *Appl. Sci.*, vol. 8, no. 5, 2018.

[11] F. Molinari, C. Caresio, and U. Acharya, "Advances in quantitative muscle ultrasonography using texture analysis of ultrasound images," *Ultrasound Med. Biol.*, vol. 41, no. 9, pp. 2520–2532, 2015.

[12] S. Seoni, G. Matrone, and K. M. Meiburger, "Robustness Analysis of Texture Features with Different Beamforming Techniques," in *IEEE Int. Ultrason. Symp. IUS*, 2020.

[13] K. W. Hollman, K. W. Rigby, and M. O'Donnell, "Coherence factor of speckle from a multi-row probe," in *IEEE Int. Ultrason. Symp. IUS*, 1999, vol. 2, pp. 1257–1260.

[14] J. Camacho, M. Parrilla, and C. Fritsch, "Phase coherence imaging," *IEEE Trans. Ultrason. Ferroelectr. Freq. Control*, vol. 56, no. 5, pp. 958–974, May 2009.

[15] E. Boni *et al.*, "A reconfigurable and programmable FPGA-based system for nonstandard ultrasound methods," *IEEE Trans. Ultrason. Ferroelectr. Freq. Control*, vol. 59, no. 7, pp. 1378–1385, 2012.

[16] S. M. Hverven, O. M. H. Rindal, A. Rodriguez-Molares, and A. Austeng, "The influence of speckle statistics on contrast metrics in ultrasound imaging," *IEEE Int. Ultrason. Symp. IUS*, no. 1, 2017.